frontiers | Frontiers in Marine Science

TYPE Original Research
PUBLISHED 11 April 2023
DOI 10.3389/fmars.2023.1115986

OPEN ACCESS

EDITED BY
Nick Pizzo,
University of California, San Diego,
United States

REVIEWED BY
Gregory Wagner,
Massachusetts Institute of Technology,
United States
Henrik Kalisch,
University of Bergen, Norway

*CORRESPONDENCE
Johannes Röhrs
johannes.rohrs@met.no

SPECIALTY SECTION
This article was submitted to
Physical Oceanography,
a section of the journal
Frontiers in Marine Science

RECEIVED 04 December 2022
ACCEPTED 22 March 2023
PUBLISHED 11 April 2023

CITATION
Röhrs J, Halsne T, Sutherland G,
Dagestad K-F, Hole LR, Broström G and
Christensen KH (2023) Current shear and
turbulence during a near-inertial wave.
Front. Mar. Sci. 10:1115986.
doi: 10.3389/fmars.2023.1115986

Current shear and turbulence during a near-inertial wave

Johannes Röhrs[1*], Trygve Halsne[1,2], Graig Sutherland[3], Knut-Frode Dagestad[1], Lars Robert Hole[1], Göran Broström[4] and Kai H. Christensen[1,5]

[1]Norwegian Meteorological Institute, Oslo, Norway, [2]Geophysical Institute, University of Bergen, Bergen, Norway, [3]Environmental Numerical Prediction Research, Environment and Climate Change Canada, Dorval, QC, Canada, [4]Department of Marine Sciences, University of Gothenburg, Gothenburg, Sweden, [5]Institute for Geoscience, University of Oslo, Oslo, Norway

Surface currents and turbulent mixing were observed during a near-inertial wave (NIW) using an accousting doppler current profiler (ADCP) and satellite-tracked drifters. Drifter trajectories sampled at three depth levels show characteristics of an Ekman solution superposed with the NIW. Velocity and dissipation estimates from the ADCP reveal strong shear with a distinct constant flux layer in between the roughness length and a critical depth at 4m. Below, a shear free slab layer performing an inertial oscillation is observed. Dissipation, as estimated from the vertical beam of the ADCP, peaks in the wave-enhanced friction layer when the current opposes the wind and wave direction. Below the constant flux layer, maximum turbulence is observed when the NIW is in a phase that is in opposite direction to the time-averaged current. During this phase, currents at various depths rapidly realign in the entire boundary layer.

KEYWORDS

near-inertial wave, surface current, turbulence, dissipation, ADCP, drifter trajectory

1 Introduction

Intense turbulent mixing characterizes the ocean surface boundary layer during wind events. The level of turbulent kinetic energy (TKE) near the surface determines momentum, energy, and tracer fluxes at the air-ocean interface (e.g. D'Asaro, 2014). As a consequence, turbulent mixing also determines how surface currents respond to wind forcing, and the vertical current profile provides a transition between the wind stress and currents at depth (Rascle et al., 2006). Whenever the wind forcing is time dependent, the ocean surface boundary layer (OSBL) responds with near-inertial waves (NIW's) during a transition to a new steady state (Alford, 2003). NIW's have frequencies slightly higher than pure inertial oscillations and contribute prominently to the internal wave spectrum (Alford et al., 2016).

NIW's are often seen as anticyclonic loops (Northern hempisphere) in drifter trajectories (Röhrs and Christensen, 2015). Changes in wind and wave forcing are often faster than the inertial period - therefore much of the upper ocean is in a state of NIW's (D'Asaro, 1985). At times, the NIW energy has a comparable magnitude to the energy in

the balanced background flow, e.g. geostrophic and wind-driven Ekman currents. Energy transfer between these reservoirs is an active field of research, and the NIW's can both feed into and drain energy from steady-state flows (Thomas and Daniel, 2020). At the same time, energy from NIWs may cascade into turbulent dissipation and thereby change dynamical balances in the mixed layer (Asselin and Young, 2020).

Turbulence in the OSBL has been studied for decades and today we have detailed understanding of how turbulent mixing and current velocities interact in a near-steady state. Prognostic numerical models can also predict turbulence and currents in non-steady states (Umlauf and Burchard, 2003), however a mechanistic description of near surface turbulence and currents in non-steady states is not widely established. Evaluation of both observations and models is required, as some of the basics in the common models, e.g. the eddy viscosity concept, are currently being revisited in light of hypothesis of counter-gradient turbulent fluxes (Milani et al., 2021).

A classic view of the OSBL is that of a *constant-flux layer*, such as in Monin-Obhukov similarity theory, where the momentum flux is assumed constant throughout the boundary layer. This assumption leads to a logarithmic ocean current profile $u(z)$, the often called *law of the wall* (LOW),

$$u(z) = \frac{u_\star}{\kappa} \log\left(\frac{z}{z_0}\right) \tag{1}$$

where $\kappa = 0.4$ is the von Kármán constant, z_0 is the roughness length and $u_\star$ is the friction velocity which is related to the surface stress τ and the density ρ by $\tau = \rho u_\star^2$. Furthermore, for a constant flux layer, the eddy viscosity will be

$$\nu_e = u_\star \kappa z \tag{2}$$

for depths greater than z_0. Technically, ν_e is not defined for depths less than z_0, but it is not uncommon to add a constant (Craig and Banner, 1994). Typically in the ocean, turbulent dynamics are described in terms of the dissipation rate of turbulent kinetic energy (TKE), ϵ, which for the constant flux layer is given by

$$\epsilon = \frac{u_\star^3}{\kappa z} \tag{3}$$

assuming a steady state and ignoring buoyancy effects (e.g. Sutherland et al., 2013).

Breaking surface gravity waves at the sea surface are known to interrupt the balance in the constant flux layer by inducing additional TKE near the surface (Craig and Banner, 1994; Sutherland et al., 2013). The decay of dissipation with depth becomes more rapid than in Eq. 3, such that $\epsilon \propto z^{-2}$ (Terray et al., 1996; Esters et al., 2018). Other studies find even stronger decay as $\epsilon \propto z^{-\lambda}$ with $-1 > \lambda > -3$ (Anis and Moum, 1995; Gemmrich, 2012). Sutherland and Melville (2015) present detailed observations of dissipation near the surface, finding that surface wave dissipation F_{ds} provides a good fit for scaling TKE dissipation in the wave-enhanced friction layer.

Dissipation has been observed to be constant in the friction layer above z_0 (Sutherland and Melville, 2015). Hence the $\epsilon \propto z^{-\lambda}$ decay starts below z_0. The transition between these vertical regimes motivates to depict the OSBL as comprising three vertical components (Röhrs et al., 2023): a near-surface friction layer where wave breaking disrupts the air-sea interface, a constant flux layer where the vertical momentum flux is approximately constant and dynamics are described by the Monin-Obhukov similarity theory, and an Ekman layer where the dynamics are dominated by τ and the Earth's rotation.

The description of turbulent mixing by Eqs. 1 and 3 assume a steady state. Often this is not the case, with currents and turbulence constantly adapting to changing winds and waves. Lewis and Belcher (2004) formulate a time-dependent solution for the current profile and ν_e, whereas NIW is part of the solution before a steady state is reached. In this study we also examine the coupling between the constant flux layer and a NIW - based on observations of currents profiles and TKE dissipation.

Common observations of ocean turbulence have relied on estimating dissipation rates using a shear-probe for the microstructure of vertical velocities (Osborn, 1980). However, retrieving dissipation rates within a few meters close to the wavy surface has proven difficult even when an upward profiling shear probe is used (e.g. Ward et al., 2014). Recent advances in Acoustic Doppler Current Profilers (ADCP) - sampling vertical velocities using a vertical beam at high frequency – allow to observe the TKE profile directly along the line of sight of the vertical beam (Guerra and Thomson, 2017; Zippel et al., 2020), however, with lower resolution than with shear probes. Herein we apply an upward looking ADCP to estimate dissipation near the surface continuously throughout a NIW cycle. The ADCP also allows to record horizontal currents simultaneously with the turbulence measurements.

In the analysis we show that velocity and dissipation reveal strong shear and a distinct constant flux layer. Below this layer, a shear free slab layer is observed. Dissipation peaks in the wave-enhanced friction layer when the current opposes the wind and wave direction. Maximum turbulence below the constant flux layer is observed when the NIW is in a phase that is in opposite direction to the time-averaged current.

This paper is structured as follows. Section 2 provides an overview of the field experiment and the type of measurements involved. In section 3 we present our data and document how the observations are processed to yield Eulerian and Lagrangian currents as well as TKE dissipation rates. In section 6 we present the vertical and temporal evolution of currents, shear and dissipation. Finally we depict the difference between vertical layers and discuss the evolution of time-dependent TKE dissipation in the presence of a NIW.

2 Data and methods

2.1 Field campaign

This research was conducted in the North Sea in June 2019 as part of the annual oil-on-water exercise arranged by the Norwegian Clean Seas Association for Operating Companies and the Norwegian Coastal Administration. A general overview of the

2019 experiment can be found in?. The main purpose of the oil-on-water exercises is to study the behavior of various types of oil on the ocean surface in realistic offshore conditions, and to test different equipment for collection and burning. As part of the 2019 exercise described in Brekke et al. (2021), two oils were left to drift freely, allowing their undisturbed drift and behavior to be studied with both remote sensing and *in situ* measurements of oil thickness.

The *Offshore Sensing SailBuoy* was deployed from the ship on 11 June at 5:54 and retrieved on 13 June at 17:39. The SailBuoy was equipped with an *AirMar weather station 200 WX* and provided wind speed, wind direction and air temperature measurements at about 0.5 m above the sea surface. The measurements compared well with the ship mast measurements when corrected for altitude using a power law correction for the atmospheric boundary layer.

Three types of ocean surface drifters were deployed covering three distinct depths (Brekke et al., 2021). The path for one of each drifter type during the experiment duration is shown in Figure 1A. An animation in the electronic supplement shows all trajectories for a period of 3 days. Two buoys with drogues centered at 15 m depth (Surface Velocity Program, SVP) showed inertial oscillations, with a period of about 13.8 hours, superimposed on a general westward drift. Two drifters with drogues centered at 60 cm depth (CODE type) showed the same inertial oscillations, but with an overall drifter velocities closer to the wind direction (south-westwards), whereas a surface drifter at the air-sea interface (iSphere) showed the same inertial oscillations superimposed with the wind direction.

A *Nortek Signature 500* 5-beam ADCP was deployed on a moored rig at 59.85 N 2.4 E from June 12 04:00 - June 13 07:00 2019. The ADCP was situated ≈ 13 m below the sea surface in an upward looking position. Maximum pitch and roll of the instrument was kept within 2°. The exact depth of the sensor varied between 13.5 m and 15 m depending on the phase of the tide. The mean water depth at the mooring location is 60 m.

The ADCP was configured to sample average horizontal currents from the slanted beams in 0.5 m vertical bins on 10 minute intervals. High frequency samples of the velocity from the vertical beam were recorded at 1 Hz in 0.5 m vertical bins, these will provide estimates of turbulent kinetic energy. In addition, a pre-set program to observe wave conditions was used to obtain surface gravity wave spectra and wave dissipation as described in Appendix A.

2.2 Meteorological measurements

Relatively strong winds characterize the time period leading up to the experiment, with winds reaching up to 11 m/s during the day before the ADCP deployment (Figure 2). This implies a well-mixed boundary layer at the onset of the experiment, with ocean forecast models indicating neutral stratification in the upper 30 m of the ocean at the experiment site (not shown).

Wind direction throughout this experiment was relatively constant from NNE with strength increasing from around 6 m/s to 14 m/s during the 26 hours observed (Figures 3A, B). Wave direction is roughly aligned with the wind, yielding significant wave height in the range of 2-3 m, shown in Appendix A.

2.3 Ocean currents

Ocean currents can be inferred from surface drifters as well as ADCP measurements. Trajectories from surface drifters (Figure 1A) and progressive vector diagrams from ADCP measurements (Figure 1B) show a similar structure. Both show a strong inertial signal – "loops" in the trajectories – in addition to a strong downwind shear in the upper 4 m. The inertial period at this latitude is 13.8 hours.

Current velocities are in a downwind phase at roughly 0 h and 13 h and in an upwind phase at about 6h and 19h (Figure 3C), hence the observed motion is well within the near-inertial frequency

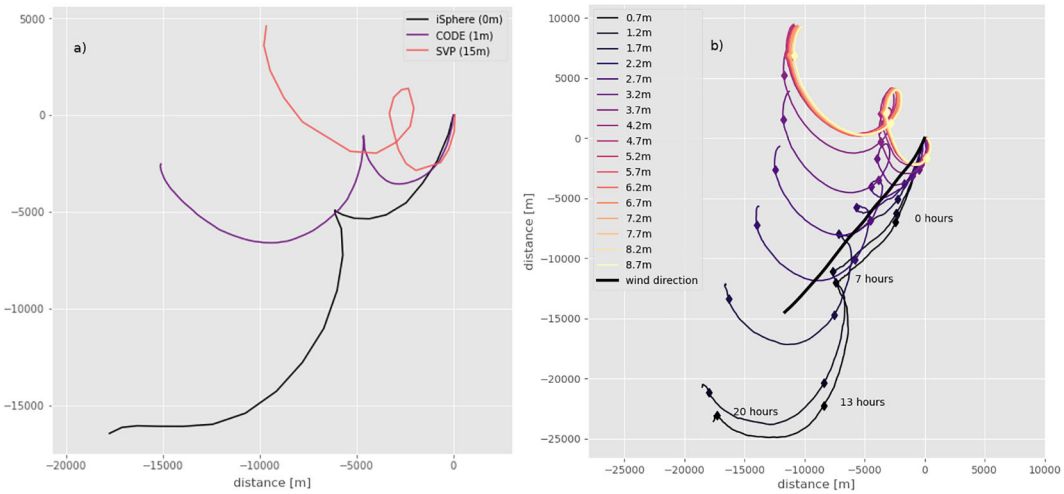

FIGURE 1
(A) Trajectories from GPS-tracked drifters at three different depths. **(B)** Progessive vector diagram of ADCP current velocities at various depths during the same time period as in **(A)**.

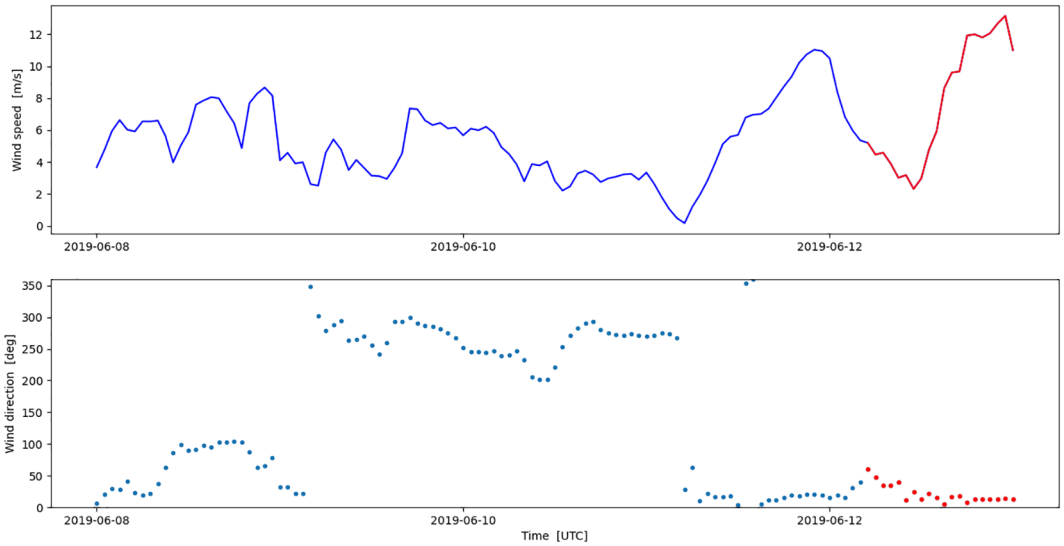

FIGURE 2
Wind speed and direction the last 7 days before the campaign period, provided by the regional weather prediction model *Arome* MEPS (Müller et al., 2017). The experiment period 12 June 04:00 UTC to ¨ 13 June 00:00 UTC is marked with red color.

band. Vertical shear is seen in the along-wind component of current velocities, while the cross-wind component exhibits very little vertical shear. Due to this shear, the surface current exhibits a downwind component throughout the NIW cycle. Transition between surface and lower level occurs between 1.2 to 3.7 m depth. From 4.2 m and below we see little variation with depth, indicating a slab layer motion performing the NIW. Averaged over a full inertial period, the vertically integrated mean current is about 90° to the right of the wind, i.e. consistent with a steady-state Ekman balance.

2.4 Turbulence measurements

Turbulence below the ocean surface is evaluated from data of the vertical ADCP beam, following the same general methodology as in Guerra and Thomson (2017), but with an additional processing step in which we reduce the signal of surface gravity waves.

For each depth in 0.5 m bins, variance spectra are calculated from the vertical velocity component w at 1 Hz. This is done for 0.5 hour segments with the method of Welch, using windows of 1200 samples with 50% overlap. We obtain energy spectra P_{ww} for the total vertical velocity that includes the orbital motion of surface gravity waves.

The ADCP is equipped with a pressure sensor sampling at 1 Hz, and this is used in a multi-step process to remove the wave orbital motion from the vertical velocity spectrum. First, the variance spectrum is calculated in the same manner as the vertical velocity spectrum, and is converted to a surface energy spectrum P_{aa}

$$P_{aa}(\omega) = P_{pp}(\omega)[\rho g \Gamma(\omega, z)]^{-2} \tag{4}$$

where P_{pp} is the pressure spectrum recorded at depth z, g is the acceleration due to gravity and $\Gamma(\omega, z)$ is the function that transforms the pressure due to wave motion recorded at depth z to the wave amplitude at the surface for each angular frequency ω,

$$\Gamma(\omega, z) = \frac{cosh\ \ k(\omega)(z + D)}{cosh\ \ k(\omega)D}, \tag{5}$$

where D is the water depth and $k(\omega)$is the wave number as calculated from the nonlinear dispersion relation for finite depth

$$\omega^2 = gk \tanh\ kD\,. \tag{6}$$

Second, from P_{aa} calculated in (4), an idealized wave spectrum is fit to the data to limit high frequency noise in the observations. Taking the peak frequency ω_p of P_{aa}, the Pierson-Moskowitz spectrum for the wind sea is calculated as

$$P_{aa}^{PM}(\omega) = \alpha g^2 \omega^{-5} e^{-\beta(\frac{\omega_p}{\omega})^4}, \tag{7}$$

using the coefficients $\alpha = 8.1e-3$ and $\beta = 0.74$ [35].

Next, the wave amplitude variance spectrum is again transferred to a vertical velocity variance spectrum for the wave motion as function of depth z:

$$P_{ww}^{wave}(\omega, z) = P_{aa}^{PM}(\omega)[\omega \Gamma(\omega, z)]^2 \tag{8}$$

Finally, the estimated wave spectra are subtracted from the total vertical velocity spectra to provide energy spectra for only the turbulent velocity component P

$$P(\omega, z) = P_{ww}(\omega, z) - P_{ww}^{wave}(\omega, z)\,. \tag{9}$$

An example of the resulting spectra for P and P_{ww} are shown in Figure 4, over a range of depths and averaged over the experiment duration. The energy spectra are shown in terms of frequency f where this is related to the angular frequency by $\omega = 2\pi f$. In

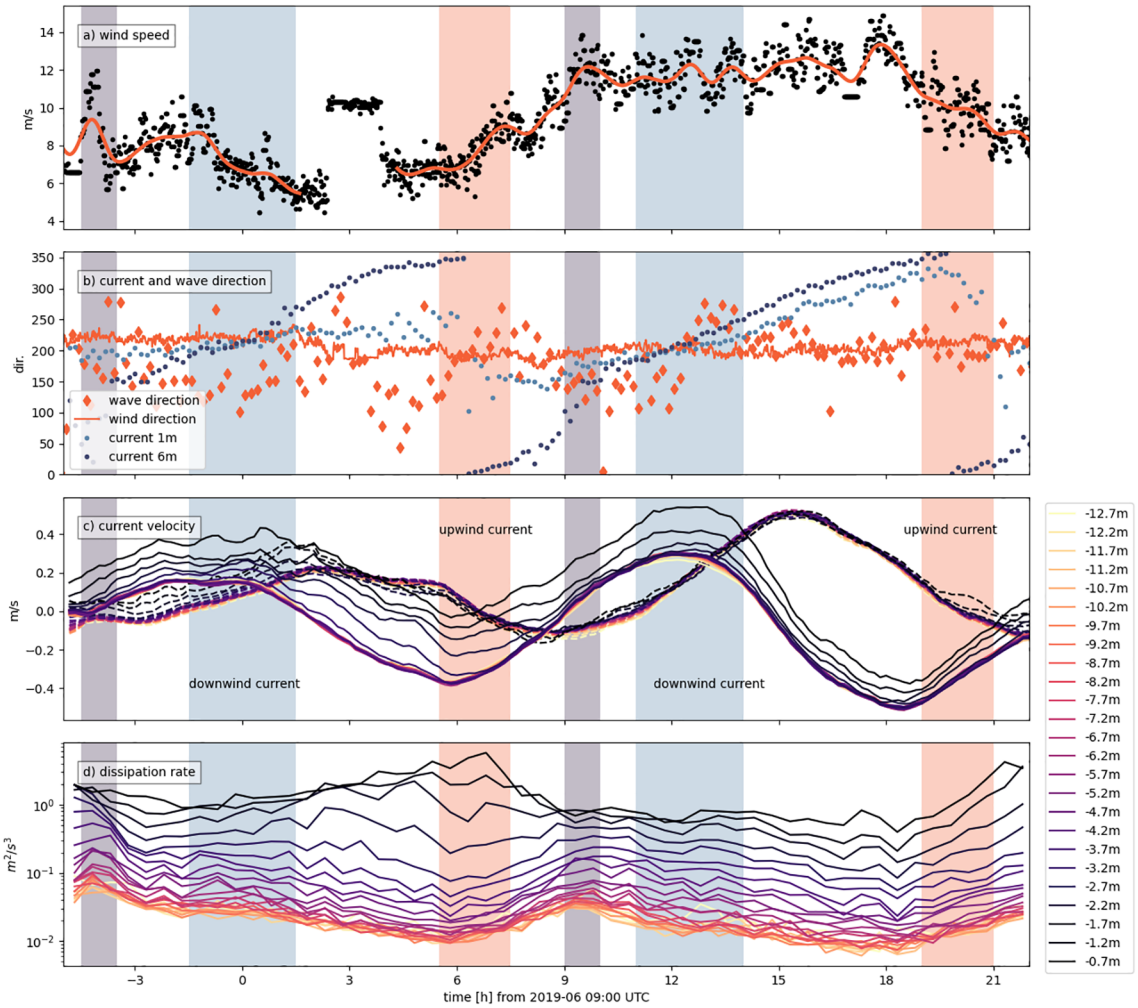

FIGURE 3
Time series of **(A)** wind speed from ship mast (dots) and low-pass filtered (line) **(B)** current, wave and wind directions, **(C)** current velocity in along-wind (solid lines) and cross-wind (dashed lines) components as function of depth, and **(D)** turbulent kinetic dissipation as function of depth. The shaded areas indicate downwind current phase (blue), upwind current phase (red) and 3 hours after upwind phase (grey).

practice, P is not entirely free of the surface gravity waves, but the steps above reduced the wave signal particularly for the energy spectra close to the surface.

A frequency range from $f_{min} = 0.2 \quad Hz$ to $f_{max} = 0.4 \quad Hz$ in the velocity spectra P in Figure 4 is identified that fulfills the property of the turbulent inertial sub-range where $P \propto f^{5/3}$ (Sreenivasan, 1995). We use the same method as [12] to calculate the dissipation rate of TKE, ϵ, from the equation

$$\epsilon = \frac{\overline{P(f) f^{5/3}} \Big|_{f_{min}}^{f_{max}}{}^{3/2}}{\alpha_\epsilon^{2/3} (\bar{u}/2\pi)} \tag{10}$$

where $\alpha_\epsilon = 0.69$ is used (Sreenivasan, 1995).

The turbulent dissipation rates are computed at 30 minute intervals at each 0.5 m depth bin. These are presented as time series in Figure 3D. The data shows that dissipation near the surface is associated with the upwind phase of the NIW. Below 3 m depth however, maximum dissipation occurs 3 hours after the surface maximum.

3 Results

3.1 Time averaged current and inertial oscillation

On average – evaluating trajectories in Figure 1 after a full inertial period – we observe downwind current velocities at the surface and a current approx. 90° to the right of the wind for the OSBL current in the Ekman layer. This is coherent with classic Ekman theory, however not with analytical solutions that require constant eddy viscosity (i.e. surface velocities at 45° to the wind). The exact direction of the interfacial surface current depends on the eddy diffusivity profile, and common solutions (e.g. Eq. 1) do not include a wave-enhanced friction layer above z_0. Looking at current directions at the roughness length $z_0 = 0.6H_s$ (Terray et al., 1996) at approx. 1.7-2.2 m in Figure 1B, we come very close to the 45° solution for classic Ekman current. The current direction at z_0 indicates the start of a constant-flux layer.

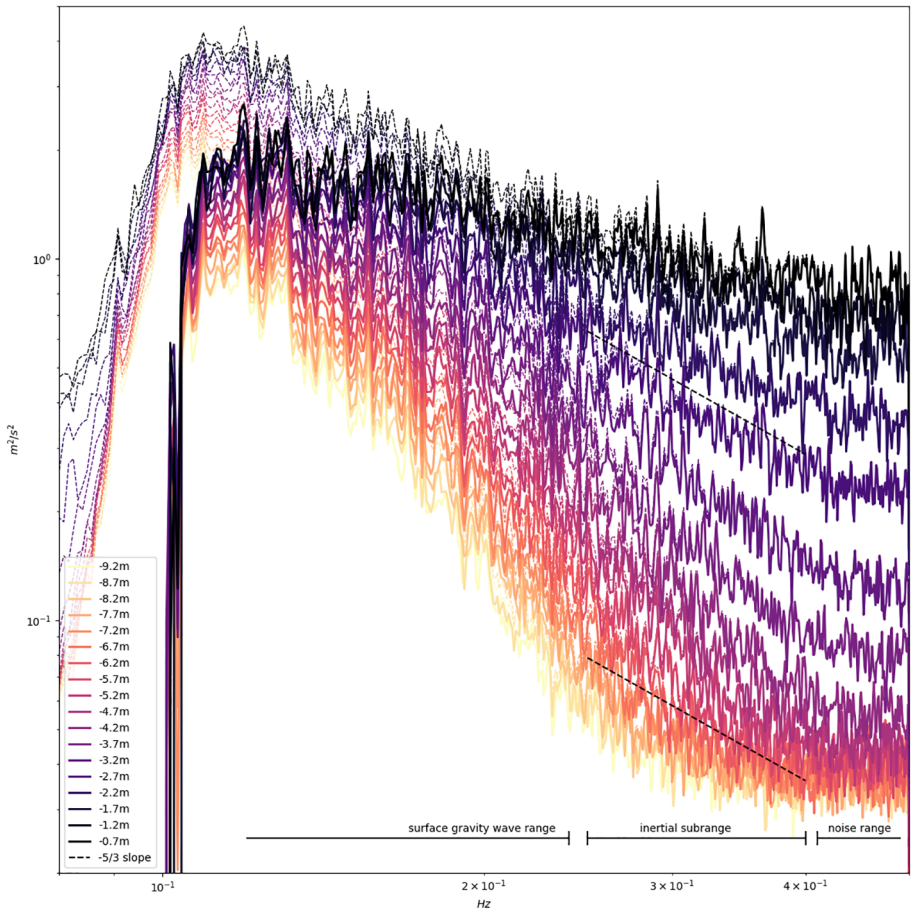

FIGURE 4
Variance spectra of vertical velocities obtained from ADCP measurements sampling at 1 Hz, for various depths below the ocean surface. The dashed lines show energy spectra obtained directly from ADCP currents. Solid lines show energy spectra where the surface gravity wave spectra is subtracted as inferred from the pressure signal at the ADCP sensor.

The direct wind-driven current at 0.7 m depth consists of a downwind current of about 0.3 m/s, superposed with the inertial current imposed by the Ekman layer. This average velocity is obtained from the total distance over two inertial periods in Fig. reffig:progvectorb. Hence the direct-wind driven current is 3% of the wind speed, consistent with the general rule of thumb for wind drift that can be reasoned by the square root of the density ratio between air and water (Wagner et al., 2022) and empirical results from spectral admittance between wind and surface currents (Röhrs and Christensen, 2015).

3.2 Vertical shear

A remarkable insight of the trajectory array in Figure 1B is that the transition between the direct wind-driven current at 0.7 m depth and the shear-free oscillating surface boundary layer current of the Ekman layer occurs over a very confined interval. At 4.2 m, this transition is completed and all deeper trajectories in Figure 1B follow a nearly identical path.

To identify dynamical regimes in these distinct layers, we evaluate a series of profiles at various time steps (Figure 5). All profiles exhibit a logarithmic velocity range $z_0 < z < z_f$, corresponding to a constant-flux layer (Eq. 1). We mark z_f as the lower range of this layer, which is at $\approx$ 4 m. Below z_f the velocity shear is negligible and the OSBL has characteristics consistent with a slab layer model (D'Asaro, 1985).

A constant flux layer is also identifiable in estimated TKE dissipation profiles, shown in Figure 6. The LOW dissipation (Eq. 3) and wave-enhanced dissipation [from Eq. 10 in (Sutherland and Melville, 2015)] are shown in black. The transition between constant ϵ near the surface (friction layer) and the power law decay of ϵ occurs at the depth $z_0 = 0.6H_s$, which is the same as for the velocity profiles. The decay of ϵ is well described by Eq.3 for the lower part of the constant-flux layer where $\epsilon \propto z^{-1}$. Closer to z_0, we see some wave-enhancement such that $\epsilon \approx z^{\lambda}$ with $-1 > \lambda > -3$.

We identified three unique dynamic regimes: i) a wave-enhanced friction layer with constant dissipation and nearly constant current, ii) a near constant-flux layer below z_0, with logarithmic current profile and $\epsilon \propto z^{-n}$, and iii) an inertial Ekman layer with slab-like motion performing a NIW with no vertical shear below a depth $z_f \approx 4$ m. The data reveal a clear distinction between these layers in terms of velocity shear and dissipation.

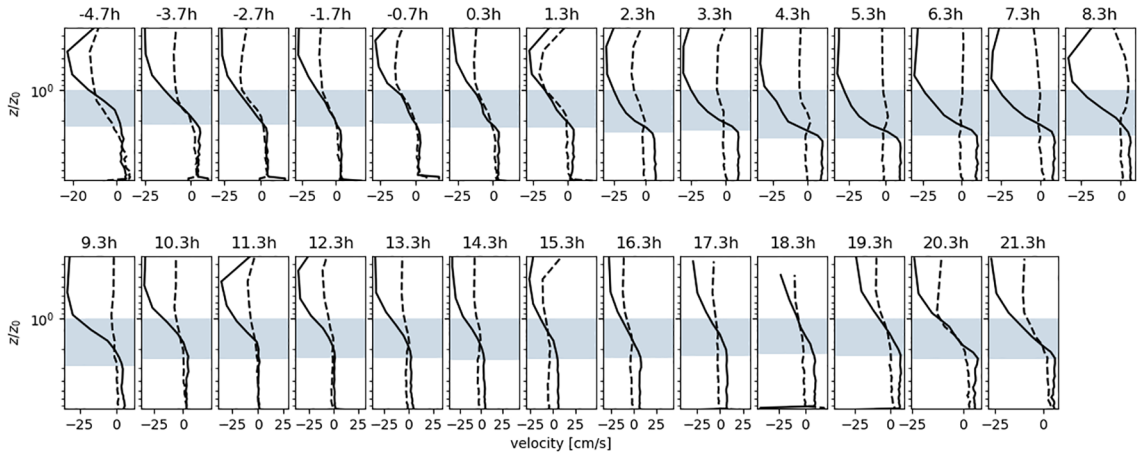

FIGURE 5
Velocity profiles on hourly intervals for eastern (dashed) and northern (solid lines) components. Shading marks the interval between z0 and zf, interpreted as constant-flux layer.

3.3 TKE from wave breaking

Surface gravity waves and the dissipation through white capping have signification implications for the OSBL (D'Asaro, 2014). Breaking waves induce TKE in the uppermost part of the OSBL, possibly explaining the observed pulses in TKE dissipation.

In Appendix A Figure A.1 we establish that the wave field during the experiment is considerably modified by the NIW,

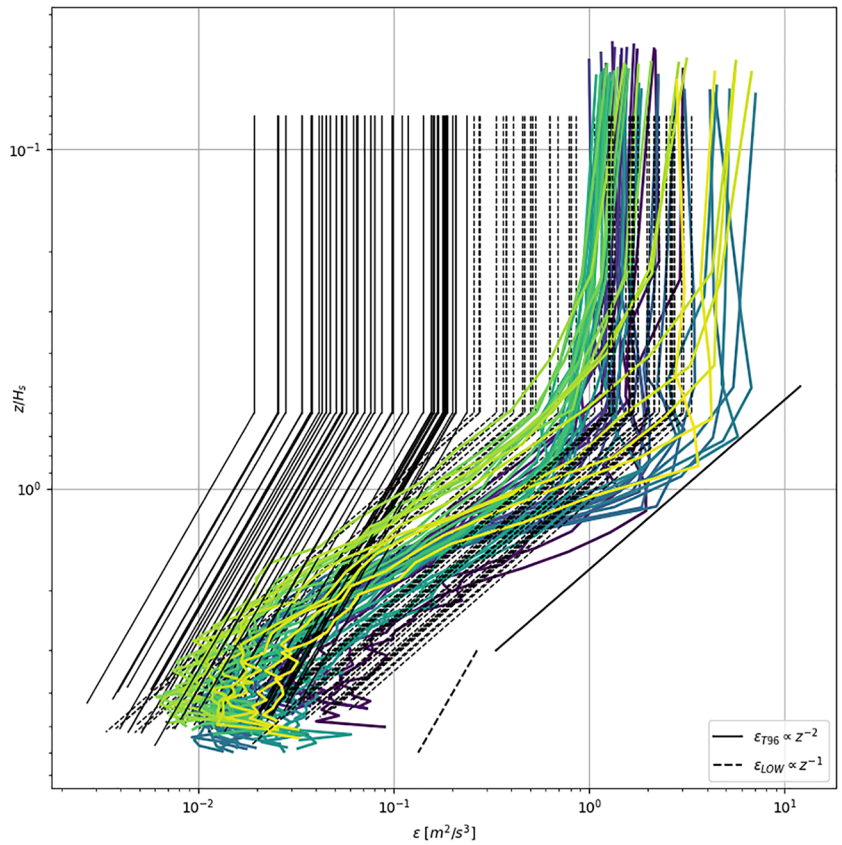

FIGURE 6
Vertical profiles of turbulent kinetic energy dissipation as obtained from vertical velocity observations. Dissipation ϵ_{LOW} as derived from wind speed and Eq. 3 is shown in black solid lines, starting at z_0 = 0.6Hs. Dashed lines use wave dissipation measurements F_{ds} (appendix A) and Eq. 10 in Sutherland and Melville (2015) to estimate ϵ as in Terray et al. (1996) for a wave-enhanced turbulence.

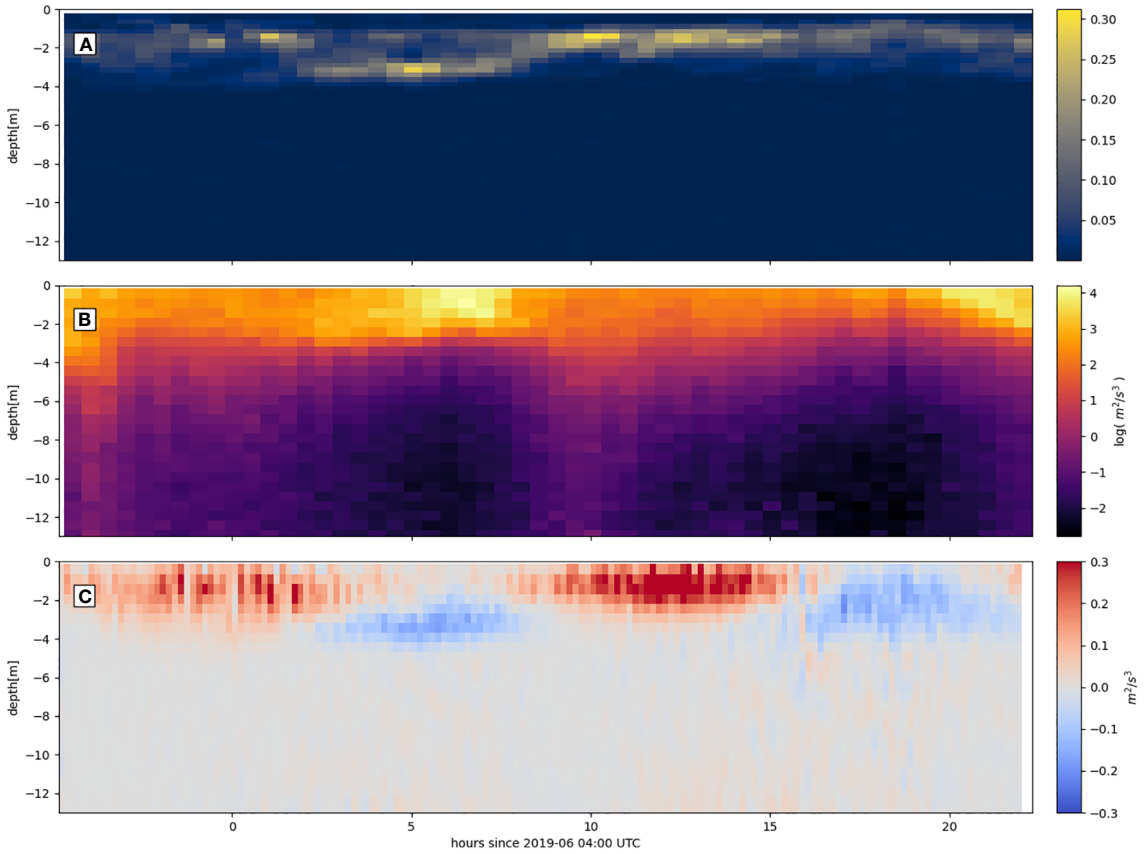

FIGURE 7

(A) Hov-Möller diagram of total vertical shear of horizontal current $\frac{\partial u_x}{\partial z}^2 + \frac{\partial u_y}{\partial z}^2$. **(B)** TKE dissipation rate based on same data is displayed in Figure 3D, referred to depth below surface. **(C)** Work exerted by shear stress on current below scaled as $W \times \rho$, as defined in Eq. 13.

causing steepening of waves during the upwind phase of the NIW. Hence we expect that increased surface wave dissipation causes pulses of TKE when the current opposes the wave propagation direction, provided that the NIW is strong enough to exceed a critical wave steepness. During the second cycle of opposing currents at t=18 h, the effective current alters the wave field enough to cause steepening of the shorter waves and associated wave breaking. In fact, we see peaks in TKE dissipation near the surface (Figure 3D), but only up to a depth $\approx z_0$.

The NIW may extract energy from the wave field at intervals of the inertial period. However, the increased TKE dissipation above z_0 does not extend into the constant flux layer. Below z_0, TKE dissipation peaks at a later time (t=-4h,9h,22h) that is not associated to changes in the surface wave field.

3.4 Vertical momentum transfer and time-dependent dissipation

Pulses of TKE dissipation above z_0 coincides with the upwind phase of the NIW as a consequence of increased relative wind stress and surface wave breaking. The TKE maxima below z_0 occur after the surface pulses, but not as a downward propagation of the surface signal. Instead, new peaks develop 3 hours after the surface peak. Figures 7A, B shows the total vertical shear and TKE dissipation as function of time and depth. With little shear below a depth of $z_f \approx 4$ m, we conclude that dissipation at depth is not primarily driven by shear production.

Assuming horizontally homogeneous flow and no stratification, the momentum equation is given by

$$\frac{\partial}{\partial t} u + 2\Omega \times u = -\frac{1}{\rho}\frac{\partial}{\partial z}\tau \tag{11}$$

where u is the velocity vector, τ is the stress vector, and Ω is the Earth's rotation vector. Taking the dot product of Eq. 11 with u yields an equation for the total kinetic energy:

$$\frac{1}{2}\frac{\partial}{\partial t}(u^2) = -\frac{1}{\rho}\frac{\partial}{\partial z}(\tau \cdot u) + \frac{1}{\rho}\tau\frac{\partial u}{\partial z}. \tag{12}$$

The terms on the right hand side represent a transport of energy and dissipation of energy, respectively. Vertical integration of Eq. 12 between depth intervals yields the total energy content in finite layers, and the first term on the right-hand-side becomes the work that is exerted by the stress τ on the velocity of the layer below:

$$W(z) = \frac{1}{\rho}\tau \cdot u, \tag{13}$$

which is evaluated at observed depths intervals shown in Figure 7C. The work of the vertical shear stress on the current of the constant flux layer is strongest positive during the downwind phase of the NIW, accelerating surface currents. During the upwind phase, the current in the constant-flux layer is decelerated. Maximum dissipation in the Ekman layer coincides with the transition from deceleration to acceleration of the current at -4h, 9h, and 22h. In these moments, current at all depths rapidly realigns in direction, as seen by the current direction at 6m depth changing quickly at $t = 9h$ (Figure 3B).

As evident from the drifter trajectories (Figure 1) and current directions (Figure 3B), particles spend considerably less time in the motion against the mean current and the strong mixing accomplishes a quick transition through this part of the NIW. It is not clear what causes this additional mixing, having excluded both shear production and surface wave dissipation. Possible reasons could be breaking of internal wave energy at the base of the mixed layer or horizontal advection of TKE, but our measurements do not provide information on these processes.

The timing of dissipation at depth in Figure 7B supports the steady state mean current by decelerating inertial currents when they are opposite to the steady state solution. The presented measurements represent the case when the mean current is directed to the right of the wind, i.e. is near a steady state balance. In the opposite case, provided that mixing at depth remains strongest when the NIW is in a phase with instantaneous currents opposite to the time-mean current, the result would be downward mixing of to-the-right-of-the-wind momentum and hence working *towards* the steady state.

4 Summary and discussion

We demonstrate the feasibility and limitations for TKE observations near the surface using a 5-beam ADCP. The observed TKE spectra exhibit strong signatures from surface gravity waves (Figure 4), and from the data it is obvious that the processing step by Eq. (9) does not succeed to remove the entire contribution from waves at low frequencies near 0.1 Hz. Due to the low sampling ratio (1 Hz) compared to turbulence observations from shear probes we also see a high noise level for frequencies above 0.4 Hz, reaching down to 0.3 Hz for depths below 4m.

The TKE dissipation signal is very strong near the surface, allowing us to estimate dissipation from 1 Hz samples in the presence of waves. This works sufficiently well near the surface in the range between 0.25 - 0.4 Hz, however below 6 m depth we suspect that noise and waves cause an overestimation of ϵ.

Despite the uncertainties of the turbulence measurements, we see a time variation at any level that is coherent with the phase of the NIW (Figure 3E). We also see a clear depth dependence throughout time that corresponds to a constant flux level with some wave enhancement (Figure 6).

The existence of a clear wave-enhanced friction layer above the constant-flux layer, as expressed by constant ϵ above z_0 in Figure 6 and in previous studies (Terray et al., 1996; Sutherland and Melville, 2015), strongly supports the concept of a roughness length z_0 that separates a friction layer from a constant-flux layer. Momentum injections from breaking waves, interruption of the air-sea interface and bubble entrainment maintain the excess momentum and energy above z_0, forcing current velocities to go straight downwind as seen in currents and drifter velocities of the uppermost observations (Figure 1).

The $\epsilon \propto z^{-2}$ dependency in the upper part of the constant flux layer (Figure 6) is indicative of wave breaking at the surface (Craig and Banner, 1994). Further below, energy from breaking waves ceases, and shear production becomes the only source of turbulence. Hence the $\epsilon \propto z^{-1}$ dissipation regime is first realized at sufficient distance from the surface. The vertical integral of the total Ekman layer being fixed at 90° or slightly more accounting for wave-current interaction (Lewis and Belcher, 2004), the overall shear in the boundary layer is fixed. With stronger shear near the surface, shear in the lower parts of the mixed layer must be lower. This could confine the lower base of the constant flux layer to a finite depth, $z_f \approx 4$ m in our case.

Stratification is not a plausible cause for the distinction of the observed layers. At wind speeds of 10 m/s and wave heights above 2 m, a pycnocline at 4 m or shallower is not sustainable given the wind history before and during the experiment. Other studies have reported such strong shear within the upper meters during high winds and in the absence of stratification (e.g. Laxague et al., 2018; Morey et al., 2018).

The presented velocity and TKE observations from the ADCP and surface drifters reveal a distinct separation of a wave-enhanced friction layer, a near constant flux layer with strong shear below the roughness length, and an inertial layer performing slab-like oscillations. Drifter trajectories perform loops in the NIW, whereby increased mixing at depth accomplishes a rapid transition through the phase of the NIW that opposes the steady-state current.

Data availability statement

The datasets presented in this study can be found in online repositories. The names of the repository/repositories and accession number(s) can be found below: https://doi.org/10.5281/zenodo.7390613, https://doi.org/10.5281/zenodo.7391898.

Author contributions

JR: Study concept, ADCP deployment, initial manuscript and editing. TH: Analysis of wave measurements, initial manuscript and editing. GS: Drifter deployment, initial manuscript and editing. K-FD: Drifter deployment, analysis of drifter data, analysis of wind data, initial manuscript and editing. LH: Drifter deployment, analysis of wind data. GB: ADCP deployment. KC:

Study concept, initial manuscript. All authors contributed to the article and approved the submitted version.

Funding

This study is financed by the Research Council of Norway, grant 237906 (CIRFA) and grant 300329 (EcoPulse).

Acknowledgments

We gratefully acknowledge the crew of R/V Helmer Hansen and the Norwegian Clean Seas Association for Operating Companies (NOFO) for enabling the measurement campaign in the North Sea. We would like to thank the reviewers for providing substantial comments improving this work.

Conflict of interest

The authors declare that the research was conducted in the absence of any commercial or financial relationships that could be construed as a potential conflict of interest.

The reviewer HK declared a shared affiliation with the author TH to the handling editor at the time of the review.

Publisher's note

Supplementary material

The Supplementary Material for this article can be found online at: https://www.frontiersin.org/articles/10.3389/fmars.2023.1115986/full#supplementary-material

SUPPLEMENTARY VIDEO FILE

Animated drifter paths for all 3 drifter pairs, whereas each pair is deployed simultaneously. The motion of the drifters highlights the slab-type motion of the OSBL.

References

Alford, M. H. (2003). Redistribution of energy available for ocean mixing by long-range propagation of internal waves. *Nature* 423, 159–162. doi: 10.1038/nature01628

Alford, M. H., MacKinnon, J. A., Simmons, H. L., and Nash, J. D. (2016). Near-inertial internal gravity waves in the ocean. *Annu. Rev. Mar. Sci.* 8, 95–123. doi: 10.1146/annurev-marine-010814-015746

Anis, A., and Moum, J. N. (1995). Surface wave–turbulence interactions. scaling epsilon near the Sea surface. *J. Phys. Oceanogr.* 25, 2025–2045. doi: 10.1175/1520-0485(1995)025<2025:SWISNT>2.0.CO;2

Asselin, O., and Young, W. R. (2020). Penetration of wind-generated near-inertial waves into a turbulent ocean. *J. Phys. Oceanogr.* 50, 1699–1716. doi: 10.1175/JPO-D-19-0319.1

Brekke, C., Espeseth, M. M., Dagestad, K.-F., Röhrs, J., Hole, L. R., and Reigber, A. (2021). Integrated analysis of multisensor datasets and oil drift simulations–a free-floating oil experiment in the open ocean. *J. Geophys. Res.: Oceans* 126, e2020JC016499. doi: 10.1029/2020JC016499

Bretherton, F. P., Garrett, C. J. R., and Lighthill, M. J. (1968). Wavetrains in inhomogeneous moving media. proceedings of the royal society of london. series a. *Math. Phys. Sci.* 302, 529–554. doi: 10.1098/rspa.1968.0034

Craig, P. D., and Banner, M. L. (1994). Modeling wave-enhanced turbulence in the ocean surface layer. *J. Phys. Oceanogr.* 24, 2546–2559. doi: 10.1175/1520-0485(1994)024<2546:MWETIT>2.0.CO;2

D'Asaro, E. A. (1985). The energy flux from the wind to near-inertial motions in the surface mixed layer. *J. Phys. Oceanogr.* 15, 1043–1059. doi: 10.1175/1520-0485(1985)015<1043:TEFFTW>2.0.CO;2

D'Asaro, E. A. (2014). Turbulence in the upper-ocean mixed layer. *Annu. Rev. Mar. Sci.* 6, 101–115. doi: 10.1146/annurev-marine-010213-135138

Esters, L., Breivik, O., Landwehr, S., ten Doeschate, A., Sutherland, G., Christensen, K. H., et al. (2018). Turbulence scaling comparisons in the ocean surface boundary layer. *J. Geophys. Res.: Oceans* 123, 2172–2191. doi: 10.1002/2017JC013525

Gemmrich, J. (2012). Bubble-induced turbulence suppression in langmuir circulation. *Geophys. Res. Lett.* 39, L10604. doi: 10.1029/2012GL051691

Guerra, M., and Thomson, J. (2017). Turbulence measurements from five-beam acoustic Doppler current profilers. *J. Atmospheric Oceanic Technol.* 34, 1267–1284. doi: 10.1175/JTECH-D-16-0148.1

Laxague, N., Özgökmen Tamay, M., Haus Brian, K., Guillaume, N., Shcherbina, A., Sutherland, P., et al. (2018). Observations of near surface current shear help describe oceanic oil and plastic transport. *Geophys. Res. Lett.* 45, 245–249. doi: 10.1002/2017GL075891

Lewis, D., and Belcher, S. (2004). Time-dependent, coupled, ekman boundary layer solutions incorporating stokes drift. *Dynam. Atmos. Oceans* 37, 313–351. doi: 10.1016/j.dynatmoce.2003.11.001

Milani, P. M., Ling, J., and Eaton, J. K. (2021). Turbulent scalar flux in inclined jets in crossflow: counter gradient transport and deep learning modelling. *J. Fluid Mechanics* 906, A27. doi: 10.1017/jfm.2020.820

Morey, S. L., Wienders, N., Dukhovskoy, D. S., and Bourassa, M. A. (2018). Measurement characteristics of near-surface currents from ultra-thin drifters, drogued drifters, and HF radar. *Remote Sens.-Basel* 10, 1633. doi: 10.3390/rs10101633

Müller, M., Homleid, M., Ivarsson, K.-I., Koltzow, M. A. O., Lindskog, M., Midtbø, K. H., et al. (2017). AROME-MetCoOp: A Nordic convective-scale operational weather prediction model. *Weather Forecasting* 32, 609–627. doi: 10.1175/WAF-D-16-0099.1

Osborn, T. R. (1980). Estimates of the local rate of vertical diffusion from dissipation measurements. *J. Phys. Oceanogr.* 10, 83–89. doi: 10.1175/1520-0485(1980)010<0083:EOTLRO>2.0.CO;2

Rapizo, H., Babanin, A. V., Provis, D., and Rogers, W. E. (2017). Current-induced dissipation in spectral wave models. *J. Geophys. Res.: Oceans* 122, 2205–2225. doi: 10.1002/2016JC012367

Rascle, N., Ardhuin, F., and Terray, E. A. (2006). Drift and mixing under the ocean surface: A coherent one-dimensional description with application to unstratified conditions. *J. Geophys. Res.: Oceans* 111, C03016. doi: 10.1029/2005JC003004

Rogers, W. E., Babanin, A. V., and Wang, D. W. (2012). Observation-consistent input and whitecapping dissipation in a model for wind-generated surface waves: Description and simple calculations. *J. Atmospheric Oceanic Technol.* 29, 1329–1346. doi: 10.1175/JTECH-D-11-00092.1

Röhrs, J., and Christensen, K. H. (2015). Drift in the uppermost part of the ocean. *Geophy. Res. Lett.* 42, 1–8. doi: 10.1002/2015GL066733

Röhrs, J., Sutherland, G., Jeans, G., Bedington, M., Sperrevik, A. K., Dagestad, K.-F., et al. (2023). Surface currents in operational oceanography: Key applications, mechanisms, and methods. *J. Operational Oceanogr.* 16, 60–88. doi: 10.1080/1755876X.2021.1903221

Sreenivasan, K. R. (1995). On the universality of the kolmogorov constant. *Phys. Fluids* 7, 2778–2784. doi: 10.1063/1.868656

Stewart, R. H., and Joy, J. W. (1974). HF Radio measurements of surface currents. *Deep Sea Res.* 21, 1039–1049. doi: 10.1016/0011-7471(74)90066-7

Strand, K. O., Breivik, O., Pedersen, G., Vikebø, F. B., Sundby, S., and Christensen, K. H. (2020). Long-term statistics of observed bubble depth versus modeled wave dissipation. *J. Geophys. Res.: Oceans* 125, e2019JC015906. doi: 10.1029/2019JC015906

Sutherland, P., and Melville, W. K. (2015). Field measurements of surface and near-surface turbulence in the presence of breaking waves. *J. Phys. Oceanogr.* 45, 943–965. doi: 10.1175/JPO-D-14-0133.1

Sutherland, G., Ward, B., and Christensen, K. H. (2013). Wave-turbulence scaling in the ocean mixed layer. *Ocean Sci.* 9, 597–608. doi: 10.5194/os-9-597-2013

Terray, E. A., Donelan, M. A., Agrawal, Y. C., Drennan, W. M., Kahma, K. K., Williams, A. J., et al. (1996). Estimates of kinetic energy dissipation under breaking waves. *J. Phys. Oceanogr.* 26, 792–807. doi: 10.1175/1520-0485(1996)026<0792:EOKEDU>2.0.CO;2

Thomas, J., and Daniel, D. (2020). Turbulent exchanges between near-inertial waves and balanced flows. *J. Fluid Mechanics* 902, 1. doi: 10.1017/jfm.2020.510

Umlauf, L., and Burchard, H. (2003). A generic length-scale equation for geophysical turbulence models. *J. Mar. Res.* 61, 235–265. doi: 10.1357/002224003322005087

Wagner, T. J. W., Eisenman, I., Ceroli, A. M., and Constantinou, N. C. (2022). How winds and ocean currents influence the drift of floating objects. *J. Phys. Oceanogr.* 52, 907–916. doi: 10.1175/JPO-D-20-0275.1

Ward, B., Fristedt, T., Callaghan, A. H., Sutherland, G., Sanchez, X., Vialard, J., et al. (2014). The air–Sea interaction profiler (ASIP): An autonomous upwardly rising profiler for microstructure measurements in the upper ocean. *J. Atmospheric Oceanic Technol.* 31, 2246–2267. doi: 10.1175/JTECH-D-14-00010.1

Westhuysen, A. (2012). Spectral modeling of wave dissipation on negative current gradients. *Coast. Eng.* 68, 17–30. doi: 10.1016/j.coastaleng.2012.05.001

Zippel, S. F., Maksym, T., Scully, M., Sutherland, P., and Dumont, D. (2020). Measurements of enhanced near-surface turbulence under windrows. *J. Phys. Oceanogr.* 50, 197–215. doi: 10.1175/JPO-D-18-0265.1

Appendix A: surface gravity waves and wave dissipation

Information about the wave field was collected in the burst mode ADCP measurements, and the wave variance spectrum and integrated spectral parameters were computed using Nortek's OceanContour (v. 2.1.2) software. This section documents how surface gravity wave dissipation F_{ds} is obtained from these measurements, and how F_{ds} is influenced by ambient surface currents of the NIW.

The wave field evolves according to the wave action balance equation

$$\frac{\partial}{\partial t}\left(\frac{E}{\sigma}\right) + \nabla \cdot \left[(u + c_g)\frac{E}{\sigma}\right] = \frac{S}{\sigma}, \tag{14}$$

where the wave action density (E/σ) is the ratio of the wave variance density and σ, and $c_g = \partial\sigma/\partial k\frac{\mathbf{k}}{k}$ is the group velocity vector. In contrast to wave variance density, the wave action density E/σ is conserved in the presence of currents (Bretherton et al., 1968). The source terms in S represents the generation (S_{in}), non-linear wave-wave interaction (S_{nl}), and dissipation (S_{ds}) of waves in an active field, such that

$$S = S_{in} + S_{nl} + S_{ds}\,. \tag{15}$$

In spectral wave models, the source terms are parameterized according to the underlying physical mechanisms and its impact on the variance spectrum. Some studies suggest that typical S_{ds} parametrizations are not capable of representing the influence of currents (e.g. Westhuysen, 2012). Rapizo et al. (2017) suggested to add a term to one of the standard parametrizations in order to account for wave field modulations due to ambient currents. More specifically, the term considers the degree of alignment between the current the wave propagation direction. The wave dissipation term reads

$$S_{ds,r} = (1 + a_3 \times \max[-\frac{u_{wdir}k}{\omega}, 0]\frac{E}{E_T})[T_1 + T_2], \tag{16}$$

where a_3 is a calibration coefficient for the energy loss due to currents and u_{wdir} is the current speed in the wave propagation direction, which is positive for aligned waves and currents. For evaluating u_{wdir}, the "effective current" should be evaluated, which takes into account the depth of influence of the various wave components (Stewart and Joy, 1974). The maximum operator limits the formulation to apply for opposing waves and currents only. E_T represent a threshold spectral density by which waves break, and the ratio will increase the dissipation for frequencies above this level. The two terms T_1 and T_2 represent the maybe most common physical parametrizations, representing a threshold behavior of wave breaking and a cumulative effect by which short wave dissipation is induced by breaking of the longer components, respectively (Rogers et al., 2012). We used $a_3 = 5$ and additional calibration coefficients for T_1 and T_2 as proposed in (Rapizo et al., 2017). The wave dissipation F_{ds} can be derived by integrating the 1D variance spectrum (Strand et al., 2020)

$$F_{ds} = -\rho g \int_{f_0}^{f_n} S_{ds,r}\,df\,. \tag{17}$$

At the beginning of the measurement period, the sea state is considered fully developed and thus estimated using a Pierson-Moskowitz spectrum (Figure A.1). The impact of u_{wdir} on the fully developed spectrum in time, only considering the effect by opposing waves and currents and ignoring wave breaking, is shown in (Figure A.1). Here, the relative growth in wave energy E/E_0 (subscript denotes initial reference value) follows the phase of the current, as waves become steeper during opposing currents (between 6–9h and 18–22h). The wave dissipation computed from Eqs. (16), (17) is shown in Figure A.1. The parameterized wave dissipation follows the significant wave height H_s (Figure A.1), and obtain a peak during the second NIW where $S_{ds,r}$ from Eq. (16) exceeds the classical parametrization (i.e. $S_{ds} = T_1 + T_2$ from Eq. 16).

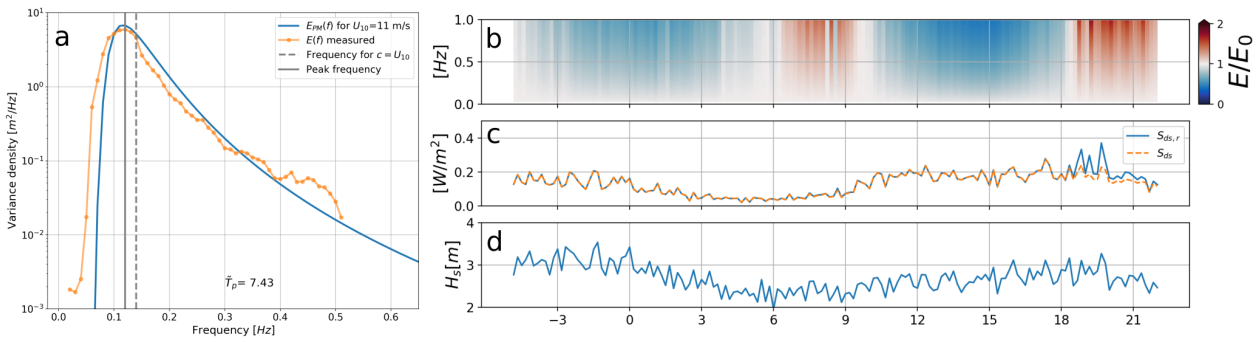

FIGURE A. 1
The impact of ambient currents on the wave field. **(A)** show the measured wave variance density spectrum at the beginning of the time series together with a computed Pierson-Moskowitz spectrum. **(B)** show the time evolution of the initial Pierson-Moskowitz spectrum in **(A)** when exposed to the effective current in the wave propagation direction uwdir. **(C)** show TKE flux computed from the measured 1D variance spectrum according to Eq. (17) for Sds,r [Eq. (16)] and without the contribution from the ambient current [Fds, i.e. a3 = 0 in Eq. (16)]. **(D)** Time series of the measured significant wave height Hs.